Ring Fault Slip Reversal at Bárarbunga Volcano, Iceland: Seismicity during Caldera Collapse and Re-Inflation 2014-2018

Esme Olivia Southern[1,1,1], Tom Winder[2,2,2], Robert Stephen White[3,3,3], and Bryndís Brandsdóttir[4,4,4]

[1]Bullard Laboratories, Department of Earth Sciences, University of Cambridge
[2]University of Cambridge
[3]Bullard Laboratories
[4]University of Iceland

January 11, 2022

Abstract

Microearthquakes reveal the kinematics of the Bárarbunga caldera ring fault; both during the 2014-2015 volcanic rifting event and gradual caldera collapse, and its subsequent, ongoing re-inflation. Manual analysis of earthquake phase arrivals has been used to produce reliable hypocenter locations with tightly constrained focal mechanisms for events both during and after the eruption. Phase arrival polarities are reversed between events that occurred during the caldera collapse and those that have occurred since. Both precise relative relocations of the seismicity and focal mechanism solutions confirm that this is due to slip reversal on the same ring fault structure. The fault planes are steeply dipping (averaging 78 ± 6°). Furthermore, the spatial distribution of aftershocks following large-magnitude post-eruptive events provides constraints on the shape and size of the fault plane and the amount of slip that typically occurs in caldera events.

Geophysical Research Letters

Supporting Information for

Ring Fault Slip Reversal at Bárarbunga Volcano, Iceland: Seismicity during Caldera Collapse and Re-Inflation 2014–2018

E. O. Southern[1], T. Winder[1], R. S. White[1], B. Brandsdóttir[2]

[1]Bullard Laboratories, Department of Earth Sciences, University of Cambridge, Madingley Road, Cambridge, CB3 0EZ, UK

[2]Háskóli Íslands, Science Institute, Sæmundargata 2, 102 Reykjavík, Iceland

Contents of this file

Figures S1 to S6 Tables S1 to S2

Additional Supporting Information (Files uploaded separately)

Captions for Figures S1 to S6 Captions for Tables S1 to S6

Introduction

This document contains a table of source parameters for each event analyzed in this study, as well as the full set of results from the calculations discussed in Section 4.2.2. It also includes full focal spheres for all events in this study, and a selection of other useful figures.

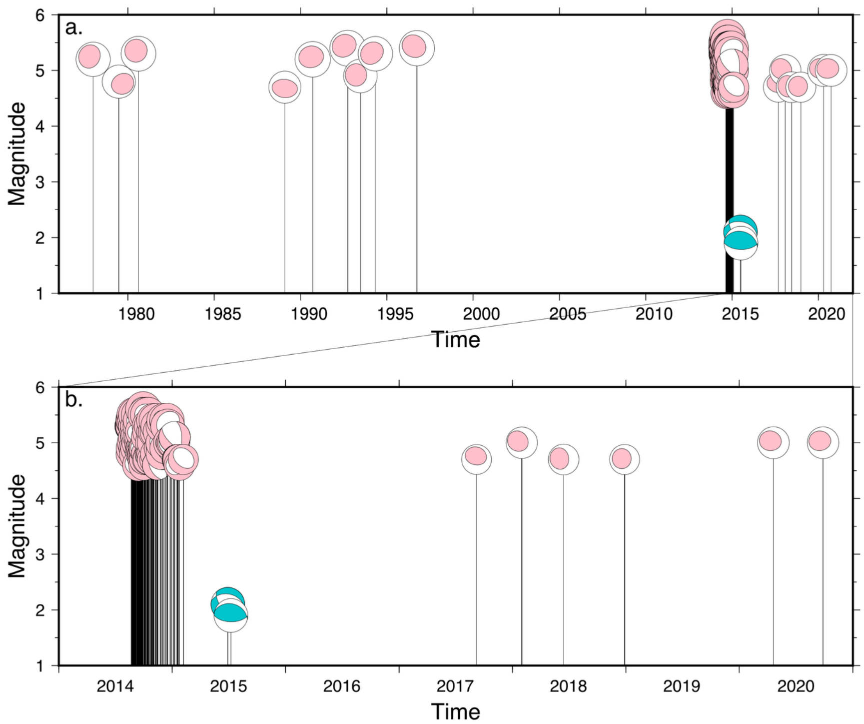

\protectFigureS1. a. Timeline showing focal mechanisms for earthquakes in the caldera region from 1976 until present. Pink focal mechanisms were published by the gCMT catalog. Although the mechanisms all display a significant CLVD component, eruptive events show a primarily normal faulting mechanism with a switch in polarity, as post-eruptive events show a reverse-faulting mechanism, in agreement with this study. Blue focal mechanisms are from Agustsdottir et al. (2019), showing the final eruptive focal mechanism and the first post-eruptive focal mechanism picked in their study. These also demonstrate a reversal in polarity from normal faulting to reverse faulting in agreement with this study. b. This is an enlargement of Fig S1.a. showing mechanisms from the eruption until present.

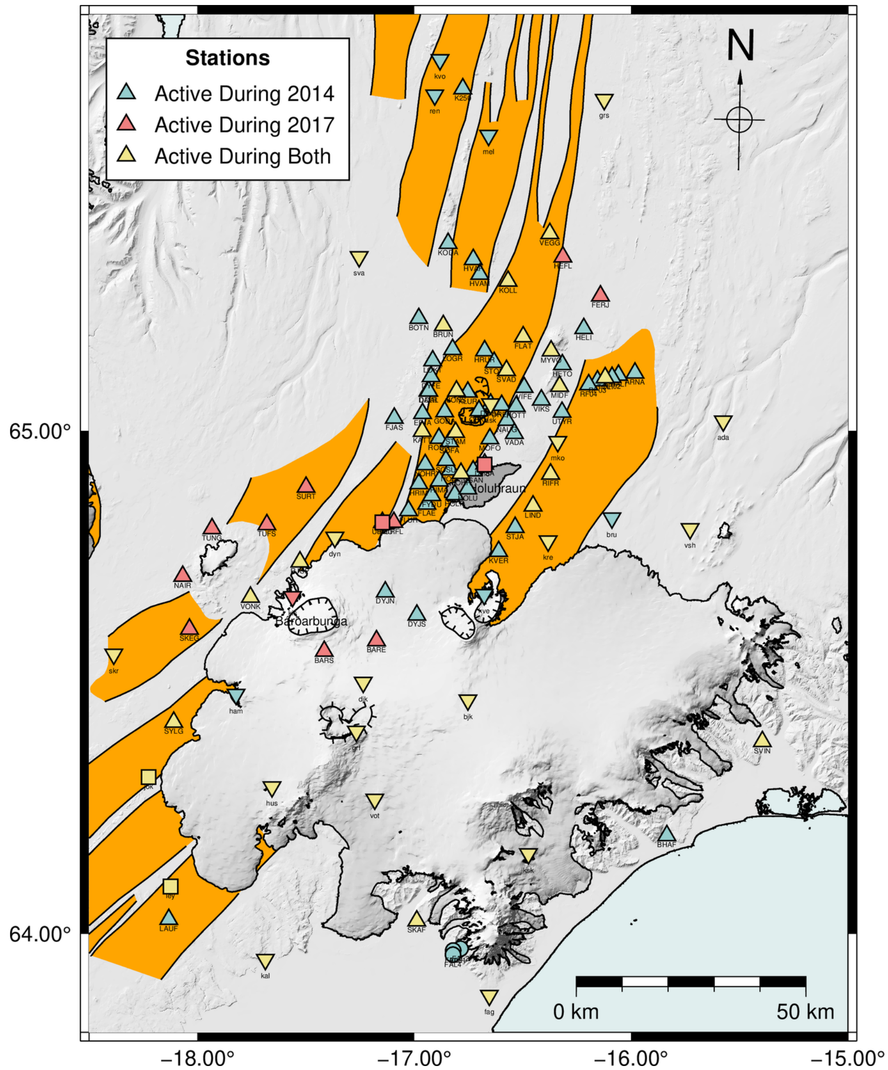

Figure S2 . Map of locations of all seismometers. Three-letter lower-case labels with inverted triangles show instruments run by the Icelandic Meteorological Office; four-letter upper-case labels with triangles show Cambridge seismometer deployments; four-character upper-case labels with circles show British Geological Survey deployments; three-letter lower-case labels with squares show University College Dublin deployments.

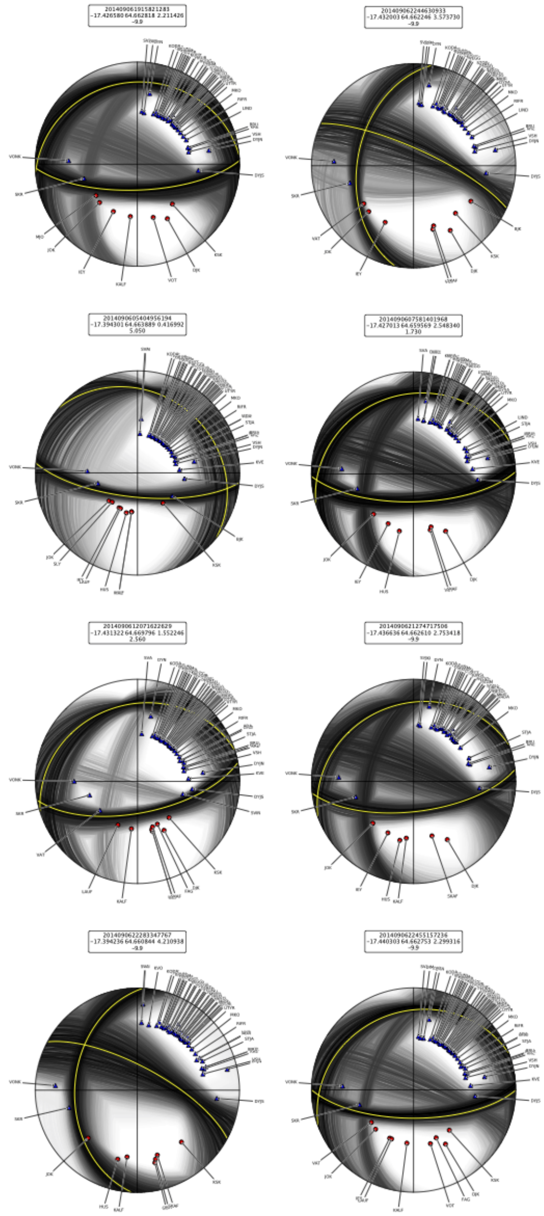

Figure S3. Full focal spheres for eruptive events. Labels indicate seismic station names; red circles denote stations with an upwards P-polarity pick; blue triangles denote stations with a downwards P-polarity pick; white triangles denote stations where an arrival time was picked but polarity couldn't be determined. The greyscale lines show possible nodal planes, with darker color indicating higher posterior probability. The yellow lines show the most probable solution.

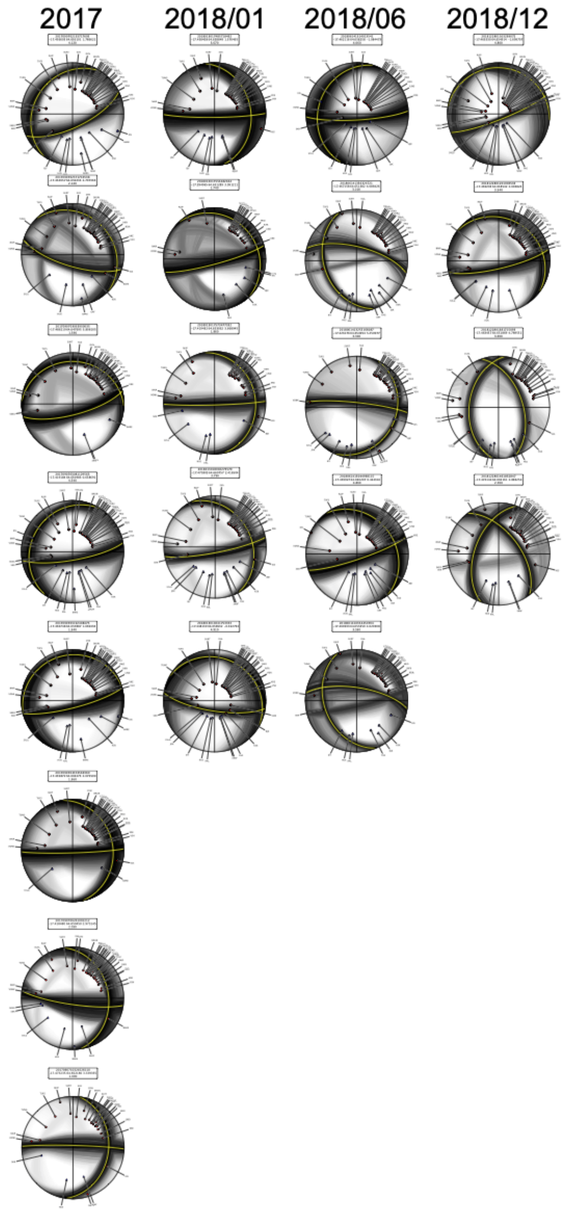

Figure S4. Full focal spheres for post-eruptive events. Labels indicate seismic station names; red circles denote stations with an upwards P-polarity pick; blue triangles denote stations with a downwards P-polarity pick; white triangles denote stations where an arrival time was picked but polarity couldn't be determined. The greyscale lines show possible nodal planes, with darker color indicating higher posterior probability. The yellow lines show the most probable solution.

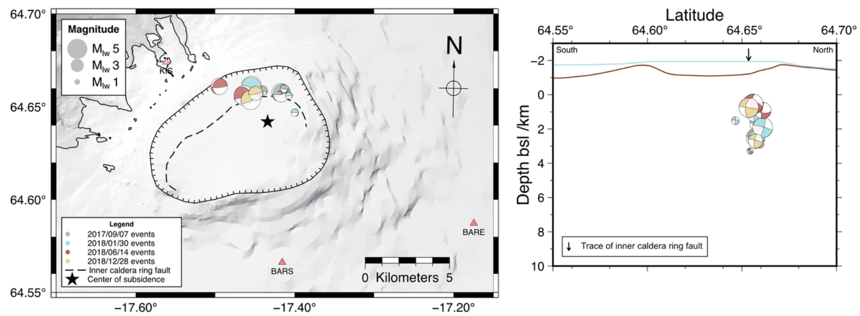

Figure S5. Alternative version of Figure 3 with no interpretation. Map shows lower hemisphere projection focal mechanisms for post-eruptive earthquakes. North-South cross section shows rear hemisphere projection focal mechanisms. Estimated trace of the inner caldera fault is based on InSAR observations by Gudmundsson et al. (2016). Location of the caldera rim and caldera bedrock surface is based on radio echo sounding by Björnsson & Einarsson (1990). Brown line in cross section shows bedrock surface, blue line shows ice surface. Cross section is displayed with no vertical exaggeration.

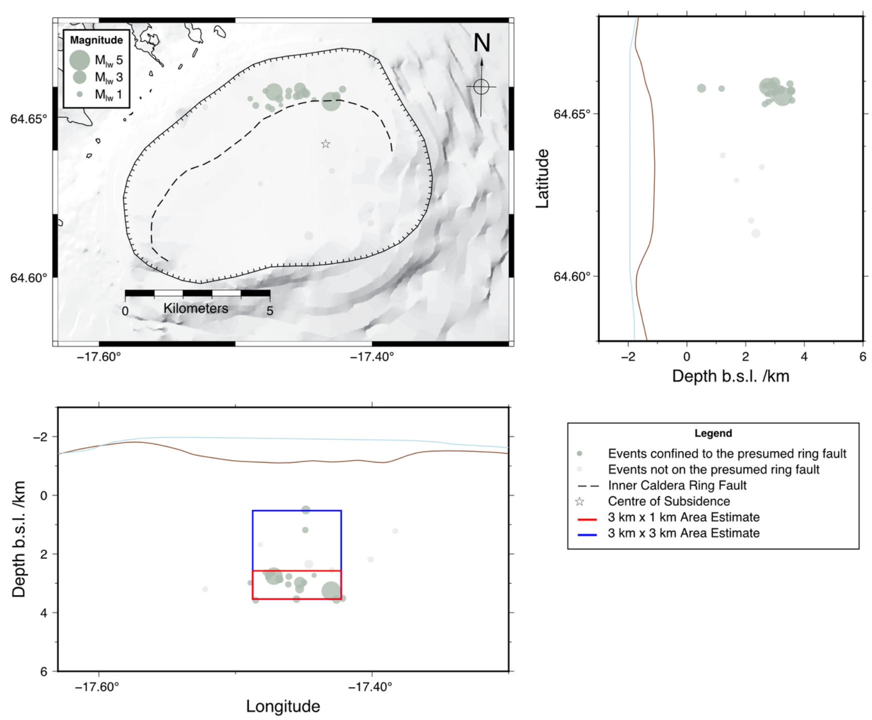

Figure S6. Manually analyzed events for the earthquake sequence surrounding the M_W 4.7 2017/09/07 event. A total of 27 events were analyzed, which includes all events above M_{lw} 1 between 2017/09/06 to 2017/09/08. Two options for fault rupture area are displayed in red and blue. The boxes in the east-west longitude-depth cross section represent two possible interpretations for rupture area of the fault plane. Estimated trace of the inner caldera fault is based on InSAR observations by Gudmundsson et al. (2016). Location of the caldera rim and caldera bedrock surface is based on radio echo sounding by Björnsson &

Einarsson (1990). Brown line in cross section shows bedrock surface, blue line shows ice surface. Cross section is displayed with no vertical exaggeration.

Hosted file

`image8.emf` available at https://authorea.com/users/560259/articles/608372-ring-fault-slip-reversal-at-b%C3%A1r%C3%B0arbunga-volcano-iceland-seismicity-during-caldera-collapse-and-re-inflation-2014-2018

\protectTableS1. Time, magnitude, location, and fault plane solution data for all 30 eruptive and post-eruptive events. Strike, dip, and rake use a Right-Hand Rule convention.

a.	μ **= 10 GPa**	μ **= 10 GPa**	μ **= 20 GPa**	μ **= 20 GPa**	μ **= 32.5 GPa**
d = 1 m	$A = 3.8$ km^2	$A = 3.8$ km^2	$A = 1.9$ km^2	$A = 1.9$ km^2	$A = 1.2$ km^2
d = 1.5 m	$A = 2.5$ km^2	$A = 2.5$ km^2	$A = 1.3$ km^2	$A = 1.3$ km^2	$A = 0.77$ km^2
b.	μ **= 10 GPa**	μ **= 10 GPa**	μ **= 20 GPa**	μ **= 20 GPa**	μ **= 32.5 GPa**
A = 3 km^2	$d = 1.25$ m	$d = 1.25$ m	$d = 0.63$ m	$d = 0.63$ m	$d = 0.39$ m
A = 9 km^2	$d = 0.41$ m	$d = 0.41$ m	$d = 0.21$ m	$d = 0.21$ m	$d = 0.13$ m
c.	**c.**	**d = 1 m**	**d = 1 m**	**d = 1.5 m**	**d = 1.5 m**
A = 3 km^2	**A = 3 km^2**	µ = 12.5 GPa	µ = 12.5 GPa	µ = 8.5 GPa	µ = 8.5 GPa
A = 9 km^2	**A = 9 km^2**	µ = 4.2 GPa	µ = 4.2 GPa	µ = 2.8 GPa	µ = 2.8 GPa

Table S2. **a.** Table shows calculated values of fault rupture area A for each combination of estimates of values using Equation 1.**b.** Table shows calculated values of average slip on the fault$d$ for each combination of estimates of values using Equation 1. **c.** Table shows calculated values of shear modulus μ for each combination of estimates of values using Equation 1.

Ring Fault Slip Reversal at Bárðarbunga Volcano, Iceland: Seismicity during Caldera Collapse and Re-Inflation 2014–2018

Authors: E. O. Southern[1], T. Winder[1], R. S. White[1], B. Brandsdóttir[2]

[1]Bullard Laboratories, Department of Earth Sciences, University of Cambridge, Madingley Road, Cambridge, CB3 0EZ, UK

[2]Háskóli Íslands, Science Institute, Sæmundargata 2, 102 Reykjavík, Iceland

Corresponding author: Esme Southern (eos24@cam.ac.uk)

Key Points:

- Fault motion reverses on the same fault planes between the eruptive and post-eruptive periods
- Tightly constrained focal mechanisms show motion on steeply dipping faults

Keywords:

Bárðarbunga, Holuhraun, caldera collapse, microearthquakes, earthquake mechanisms

Abstract

Microearthquakes reveal the kinematics of the Bárðarbunga caldera ring fault; both during the 2014–2015 volcanic rifting event and gradual caldera collapse, and its subsequent, ongoing re-inflation. Manual analysis of earthquake phase arrivals has been used to produce reliable hypocenter locations with tightly constrained focal mechanisms for events both during and after the eruption. Phase arrival polarities are reversed between events that occurred during the caldera collapse and those that have occurred since. Both precise relative relocations of the seismicity and focal mechanism solutions confirm that this is due to slip reversal on the same ring fault structure. The fault planes are steeply dipping (averaging 78 ± 6°). Furthermore, the spatial distribution of aftershocks following large-magnitude post-eruptive events provides constraints on the shape and size of the fault plane and the amount of slip that typically occurs in caldera events.

1 Introduction: Geological setting and the 2014–2015 eruption

Bárðarbunga is a large, basaltic central volcano in Iceland's Eastern Volcanic Zone (Jóhannesson & Sæmundsson, 1998), situated beneath the Vatnajökull ice cap. The Bárðarbunga volcanic system has been highly active in the Holocene, with at least 26 eruptions in the last 11 centuries (Brandsdóttir & Pálsson, 2014; Larsen & Gudmundsson, 2015). Bárðarbunga itself comprises a 500–800 m deep ice-filled subglacial caldera, approximately 10 km across, with a fissure swarm about 190 km long and up to 25 km wide (Larsen & Gudmundsson, 2015). Seismic activity has been detected throughout modern recording history, notably increasing over a period of 20 years leading up to the nearby Gjálp eruption in 1996 (Bjarnason, 2014).

In August 2014, melt intruded 48 km from Bárðarbunga along a lateral dike, first propagating 5 km towards the southeast before turning north-eastward, and eventually erupting at Holuhraun (Fig. 1). During the six month long eruption, 1.5 km^3 of magma was erupted at Holuhraun (Pedersen et al., 2017), and Bárðarbunga caldera collapsed as melt flowed out from beneath it (Gudmundsson et al., 2016). Intense seismicity accompanied the collapse and was recorded by a dense local seismic network (Ágústsdóttir et al., 2019). This included more than 75 $M_W > 5$ earthquakes (Gudmundsson et al., 2016).

Caldera collapse events have rarely been recorded and studied in such detail as that associated with the 2014 – 2015 Bárðarbunga-Holuhraun volcanic rifting episode. Geodetic data provide important constraints on the dynamics and geometry of the collapse; Gudmundsson et al. (2016) reported 65 m of incremental, highly asymmetric subsidence at Bárðarbunga during the eruption from GPS measurements and radar profiling. A pair of synthetic aperture radar (InSAR) images spaced just one day apart, and capturing a M_W ~ 5 earthquake, identified the trace of a possible inner caldera ring fault close to its northern rim (Fig. 1). Further work by Ágústsdóttir et al. (2016, 2019) and Woods et al. (2019) has provided detailed analysis of the seismicity along the dike path and within the caldera throughout the duration of the eruption. In the caldera, seismicity is concentrated on the northern rim, supporting the inference from geodetic observations that the collapse was highly asymmetric. Ágústsdóttir et al. (2019) report normal faulting occurring during the eruption on steeply inward-dipping faults, striking sub-parallel to the caldera rim. This is interpreted as representing a combination of piecemeal and trapdoor style collapse mechanisms (Acocella et al., 2007).

There have been several reports that the polarity of fault motion changed after the eruption ended. Cross-correlation of similar earthquake waveforms observed on a single seismic station shows a reversal in polarity as early as 2 months after the end of the eruption (Jónsdóttir et al., 2017), and source parameter inversions derived from fitting regionally recorded earthquake waveforms show a similar result (Rodríguez-Cardozo et al., 2019). In addition, between the end of the eruption and September 2020, the Global Centroid Moment Tensor (gCMT) project (Dziewonski et al., 1981; Ekström et al., 2012) has reported six large-magnitude events (M_w 4.7 and above) in the Bárðarbunga area, which all show reversed polarity compared to those seen during the eruption (Supplementary Fig. S1). Geodetic data also provides evidence of caldera inflation initiating shortly after the eruption ceased (Li et al., 2021). Li et al. (2021) test different models to evaulate the roles of both renewed inflow of magma and viscoelastic relaxation following magma withdrawal in driving the observed surface deformation. They conclude that both processes are likely important, with a combination of magma inflow to a sill at 10 km depth and slip on the caldera ring fault providing a good fit to the observations.

However, these studies leave several open questions, most importantly whether this reversal in deformation represents a mirror image of that during the eruption, or a more complex evolution. The limited hypocentre resolution in the aforementioned studies makes it impossible to answer this definitively. Furthermore, the geometry of the caldera ring fault remains an open question (Ágústsdóttir et al., 2019), and this continued seismicity provides an opportunity to further investigate this.

In this study we focus on two co-located large earthquakes on the northern caldera rim, and their associated fore and after shocks; one in 2014, during the eruption, and the second from 2017, during the subsequent reinflation. The 2017 earthquake was chosen because the seismometer array was particularly dense at this time, including several temporary seismometers on the ice cap close to the caldera (Fig. 1). This should provide an excellent opportunity to calculate precise locations and tightly constrained fault plane solutions for earthquakes of a range of magnitudes. The two mainshocks are in the same location within uncertainties, and apparently result from movement on the same fault, though the eruption (deflation) event has a normal faulting mechanism and the re-inflation event a reverse faulting mechanism. We also present hypocenter and fault plane solutions for foreshocks and aftershocks to each large earthquake in Bárðarbunga between 2015-2018 reported in the gCMT catalogue, to investigate the mechanism and reactivation of caldera faulting after the eruption.

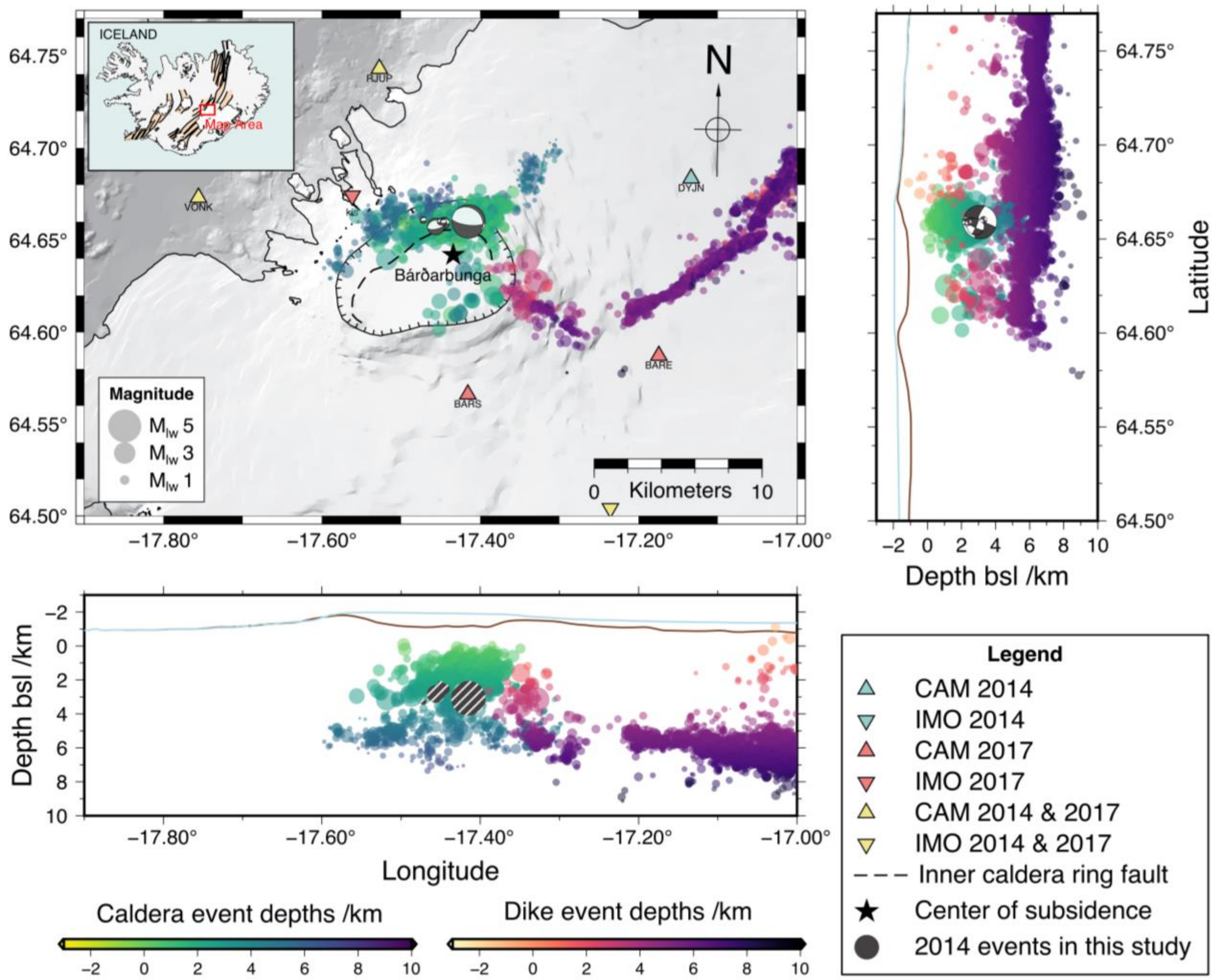

Figure 1. Map and cross sections show relatively relocated seismicity during the August 2014 dike propagation and 2014-15 caldera collapse (from Ágústsdóttir et al., 2019) colored by depth. Focal mechanisms for eight eruptive events are shown, all of which display normal faulting, in lower hemisphere projection in map view and rear hemisphere projection in the north-south cross section. Triangles mark seismometers, star shows center of subsidence, dotted line denotes inner caldera ring fault. Inset map shows the location of the study area in Iceland. Estimated trace of the inner caldera fault is based on InSAR observations by Gudmundsson et al. (2016). Location of the caldera rim and caldera bedrock surface is based on radio echo sounding by Björnsson & Einarsson (1990). Brown line in cross section shows bedrock surface, blue line shows ice surface. Cross sections are displayed with no vertical exaggeration.

2 Seismic Data

Continuous seismic data were recorded on a dense local network of three-component broadband seismometers operated by the University of Cambridge, supplemented by seismometers from the Icelandic Meteorological Office (IMO), the British Geological Survey (BGS) and University College Dublin (UCD) (Supplementary Figure S2). At its maximum, up to 72 seismometers were recording at once. We studied events from during the eruption reported in the catalog of Ágústsdóttir et al. (2019), and used the QuakeMigrate software (Winder et al., 2020), to detect and locate earthquakes within two days either side of those reported in the gCMT catalog in the period after the eruption ended. We use the same regional one-dimensional velocity model, from Ágústsdóttir et al. (2016). Earthquake magnitudes are derived from the gCMT catalog (M_W) where available, or from the IMO's Southern Iceland Lowlands (SIL) network catalog (M_{lw}) where not (Jónasson et al., 2021; Rögnvaldsson & Slunga, 1993).

All events were analyzed manually, by picking P- and S-wave arrival times and assigning P-wave polarities using the Pyrocko Python package and Snuffler toolbox (Heimann et al., 2017). Filtering of the waveforms was kept to a minimum; if the arrival remained unclear with a highpass filter of more than 4 Hz and lowpass of less than 20 Hz, a pick was not made. Polarity was assigned with no filtering. Hypocentre locations were calculated using the NonLinLoc software (Lomax et al., 2000). Focal mechanisms were then obtained by inversion using MTfit (Pugh & White, 2018). We found that a good fit to the data was achieved to all events with inversions constrained to the double-couple (DC) moment tensor space, despite including observations from an unusually dense local seismic network.

Hypocentres were further refined by relative relocation using hypoDD (Waldhauser and Ellsworth, 2000) with uncertainty on the relative relocations showing improvement of around an order of magnitude compared to absolute locations. Absolute locations have a mean uncertainty of 0.59 km laterally and 1.16 km in depth, whereas relative relocations have a mean uncertainty of 38 m laterally and 129 m in depth. Depth is generally the least well constrained parameter, largely due to the lack of stations directly above the events. Improvement in the density of station coverage, particularly during 2017 when stations BARS and BARE were active on the surface of the glacier (Fig. 1, Supplementary Fig. S2), significantly improves both absolute and relative relocation constraint for the 2017 earthquake sequence.

The Cambridge network yields an earthquake catalog with a magnitude of completeness M_C ~1.2 in this area (Greenfield et al., 2020). The global Centroid Moment Tensor (gCMT) catalog has an average M_C ~5.0 (Ekström et al., 2012).

3 Results

A total of 30 events were manually analyzed in this study, of which all but six events (two eruptive and four post-eruptive), show east-west striking nodal planes and sub-vertical dip-slip faulting. Source parameters for each event are displayed in Supplementary Table 1, and full focal spheres are shown in Supplementary Figures S3 (eruptive events), and S4 (post-eruptive events).

The six focal mechanisms which do not fit this consensus are all from events which show a large shift to shallower depth when relatively relocated. The polarity picks at common stations are identical to those for events with better constrained locations, indicating that the different focal mechanism results are caused by differing take-off angles. As these only form a minority of the dataset, and are likely caused by errors in the absolute depth estimates, they are not discussed further in this paper.

3.1. Eruption period (August 2014 – February 2015)

Six events from the eruptive period produced reliable fault plane solutions: a M_W 5.1 event on 2014/09/06, with particularly good azimuthal station coverage, alongside the five next-largest events in the following two days (Fig. 1). Around 4000 events, extending down to 6 km depth below sea level (bsl), were automatically detected and located within the caldera during the eruptive period by Ágústsdóttir et al. (2019), Figure 1.

Most of the recorded seismic activity and moment release has been concentrated on the north side of the caldera throughout the eruptive and post-eruptive stages (Ágústsdóttir et al. 2019). The six relatively relocated hypocenters lie on or near the northern caldera rim in map view, and between 2–4 km depth bsl in cross section (noting that the caldera rises to 2009 m above sea level, so they are 4–6 km below the surface).

The six well-constrained focal mechanisms show a steeply dipping nodal plane striking east-west between 078 – 097°, subparallel to the northern caldera rim, and dipping between 65 – 72°. They all indicate downwards motion on the inner side of the caldera ring fault. In cross-section, rear hemisphere projection focal mechanisms demonstrate this more clearly, with one nodal plane consistently dipping steeply to the south, into the caldera; this nodal plane is interpreted as the fault plane, fitting best with models of caldera collapse (Acocella et al., 2007). Further discussion on the fault plane and its geometry is provided in Section 4.

3.2. Comparison of co-located earthquakes during and after the eruption

The most significant result of this study is highlighted in Figure 2. Figure 2a shows a focal mechanism and first-motion waveforms for a M_W 5.1 event in September 2014, during the eruption, and Figure 2b shows the same for a M_W 4.7 in September 2017, during the re-inflation period. Both focal mechanisms are tightly constrained, and share a very similar fault plane striking approximately east-west. They demonstrate an exact polarity switch from normal to reverse faulting. First-motion polarities at all stations common to both events are opposite between the two earthquakes. The 2017 event has better constraint on the nodal planes due to better azimuthal station coverage, leading to a smaller spread of possible fault plane solutions, particularly for the auxiliary plane (which defines the slip vector).

Figure 2c shows Pressure (P) and Tension (T) axes on polar stereonets for the 6 eruptive events, and Figure 2d for the 18 post-eruptive events. These demonstrate that the reversal in polarity between the eruptive and post-eruptive periods is consistent across all events in this study.

3.3. Post-Eruption period (March 2015 – December 2018)

Post-eruptive seismic activity within the caldera includes six events of sufficiently large magnitude to be detected teleseismically and included in the gCMT catalog. We investigated four of these that occurred between 2017 and 2018, and microearthquakes that occurred within two days before and after each. The results are shown in Figure 3.

A total of 18 well-constrained focal mechanisms were obtained for earthquakes during this period. As for the eruptive period, the post-eruptive focal mechanisms all show a steeply dipping nodal plane striking east-west parallel to the caldera rim in map view, again interpreted as the fault plane. Strikes range from 065 - 104°. In cross-section, rear hemisphere projection focal mechanisms clearly show the steep fault planes, with an average dip of 81 ± 5°.

During the post-eruptive period, all 18 well-constrained focal mechanisms show upwards motion on the inner side of the caldera ring fault, indicating reactivation of the caldera ring fault, which earlier dropped down during the eruptive phase. Two of these show an outward dipping fault plane at 81 – 82°, but the other 16 are inward dipping between 70 – 88°.

3.4. Fore- and aftershocks to the September 2017 M_W 4.7

The sequence of earthquakes around the M_w 4.7 event on 2017/09/07 was examined in more detail, to take advantage of the excellent station coverage available at that time; ice stations BARE and BARS were active, as well as nearby KIS, DYN and DJK, considerably improving coverage both in terms of proximity and azimuth compared to the 2014 events. Most importantly, KIS is < 2 km from the northern caldera rim, greatly enhancing location constraint, particularly in depth. All events with $M_{lw} > 1$ between 2017/09/06 and 2017/09/08 were manually located, totalling 27 events (Supplementary Fig. S6), and contributed to our estimate of fault rupture area, discussed further in Section 4. The study of this large earthquake and its associated events enabled us to calculate tightly constrained focal mechanisms for smaller events in addition to larger ones, which is significant, as the point-source approximation our methods rely on is more appropriate for smaller events that cannot usually be studied as closely. We find the small events to be very consistent both with one another and with the larger events, which allows us to estimate the extent of the fault plane which slipped during the large event, as discussed below.

3.5. Fault plane geometry from relative relocations

During the post-eruptive period, seismic activity remained concentrated in the north of the caldera, though the number and average magnitude of events are much smaller than during the eruption (Ágústsdóttir et al., 2019). The epicentral hypocentral constraint is improved compared to the eruptive period, due to improved network geometry. Depth uncertainty is similar for both periods. Most hypocenters relatively relocate within 0 – 4 km depth b.s.l. (2 – 6 km below the surface). Following relative relocation, the pattern of hypocenter locations collapses into a cluster just a few hundred meters across.

With the improved location constraint achieved in this study, we are able to use the relative relocations as a second method to investigate the caldera ring fault geometry. A range of best-fitting planes through the hypocenters was fitted using jack-knife testing (Tukey, 1958), each with steep dip in cross section, between 83° southwards into the caldera and 85° northwards, represented by the gray shaded area in Figure 3b. (Supplementary Figure S5 shows a version of Figure 3 with no interpretation).

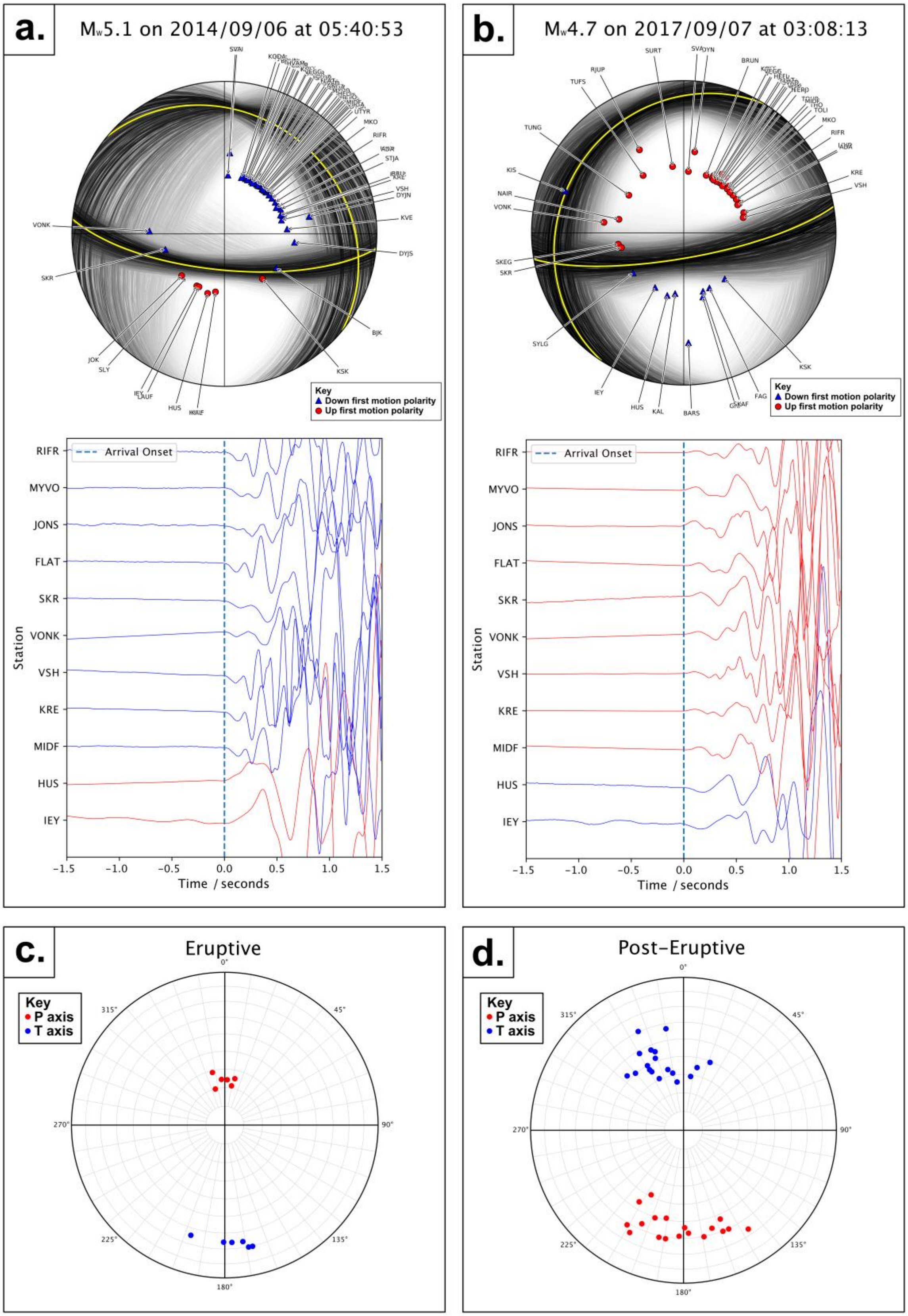

223 **Figure 2. a.** Focal mechanisms and first-motion waveforms for a M_W 5.1 eruptive event on

2014/09/06. **b.** Focal mechanisms and first-motion waveforms for a M_W 4.7 post-eruptive event on 2017/09/07. These highlight the polarity reversal in P-wave arrivals. Greyscale lines show possible nodal planes, with darker color indicating higher posterior probability and yellow lines showing the best-fit planes reported by MTfit. The fault plane, interpreted as the east-west-striking plane, is highly similar for the two events, but the first-motion polarity at all stations common to both events is reversed, as seen in the vertical component P-wave first-motion waveforms. Seismometer locations are shown in Supplementary Figure S2. **c.** Pressure (P) axes (red) and Tension (T) axes (blue) for all eruptive events analyzed in this study. **d.** Pressure (P) axes (red) and Tension (T) axes (blue) for all post-eruptive events analyzed in this study.

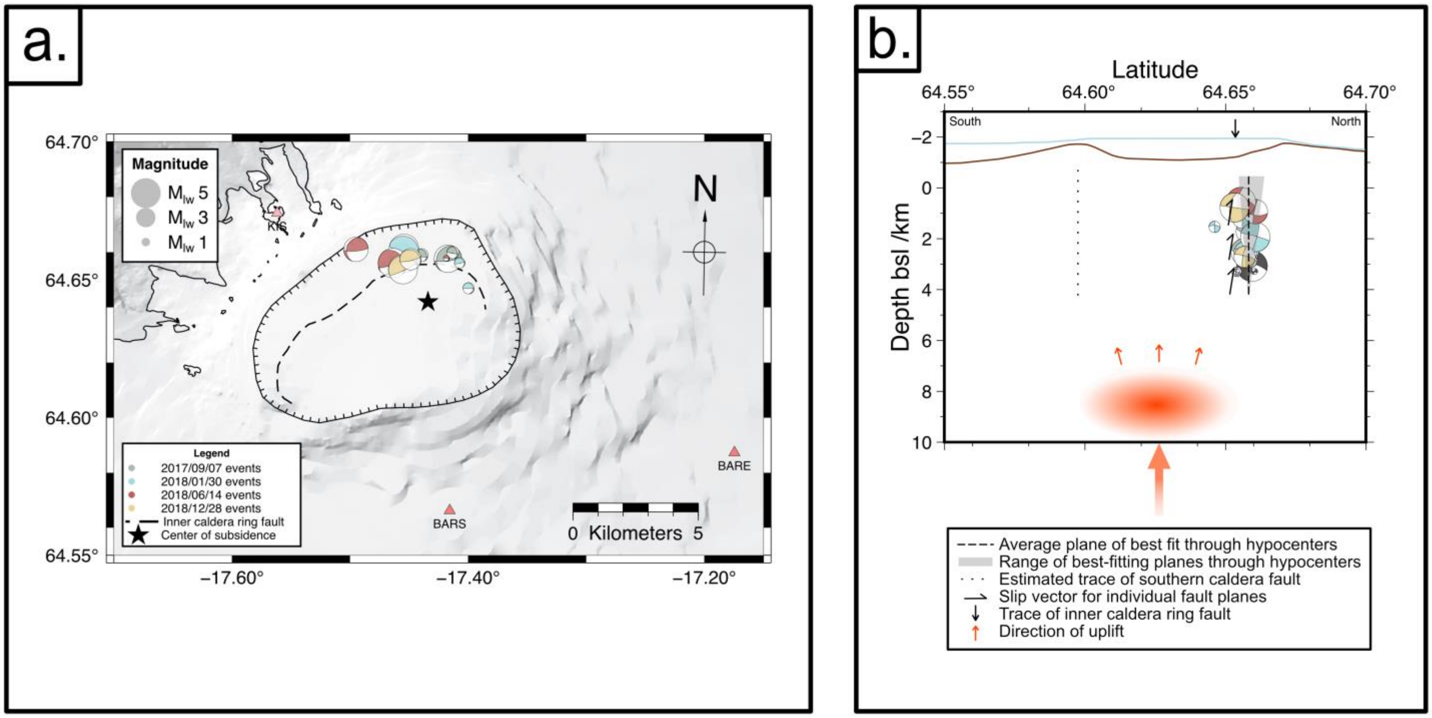

Figure 3. a. Map of lower hemisphere projection focal mechanisms for post-eruptive earthquakes. Estimated trace of the inner caldera fault is based on InSAR observations by Gudmundsson et al. (2016). **b.** North-South cross section through the centre of subsidence. Rear hemisphere projection focal mechanisms highlight the steeply inward dip of the fault planes, all of which show upwards motion of the southern (inner caldera) side of the fault. Location of the caldera rim and caldera bedrock surface is based on radio echo sounding by Björnsson & Einarsson (1990). Estimated trace of southern caldera fault in cross section is based on seismicity distribution found by Ágústsdóttir et al. (2019). Brown line in cross section shows bedrock surface, blue line shows ice surface. Cross section is displayed with no vertical exaggeration.

3.6. A note on Double-Couple (DC) vs Compensated Linear Vector Dipole (CLVD) Moment Tensor solutions

All well-constrained focal mechanisms in this study (consisting of earthquakes with M_W 5.1 and smaller) could be fit by a purely Double-Couple (DC) fault plane solution, indicating slip on a planar fault. This contrasts with the mechanisms for the larger events published in the gCMT catalog, which contain a significant compensated linear vector dipole (CLVD) component, and a possible volumetric contribution. Ágústsdóttir et al. (2019) also found most focal mechanisms to be purely DC, though a few required a CLVD component. However, the estimated fault rupture area for most earthquakes in this study (discussed further in Section 4) may be sufficiently small that it does not involve rupture of a significantly curved surface and so, in this case, quasi-planar fault slip would mean that the sources are likely to be DC. This is supported by the results of Rodríguez-Cardozo et al (2021), who find that moment tensor solutions for earthquakes during the caldera collapse show larger CLVD components for larger magnitude events.

4. Discussion

4.1. Caldera ring fault slip reversal

The most significant result of this study is the mirror-image reversal of earthquake focal mechanisms between the eruptive and post-eruptive periods (Figure 2), indicating downward motion on the south side of the caldera ring fault during the eruption and upwards motion during the post-eruptive period. This polarity reversal is also observed in moment tensor solutions from the gCMT catalog, and suggested by results reported by Ágústsdóttir et al. (2019) (Supplementary Fig. S1), and corresponds with observations from InSAR and GPS measurements from Li et al. (2021) indicating that the caldera is now re-inflating. The similarity of hypocenter locations and orientations of fault planes between the two periods suggests that the mechanism of reversal is simple re-activation of the same fault or group of faults around the caldera rim.

This reversal is partly attributed to re-inflation of the magma storage region beneath the caldera (Li et al., 2021). The subsidence during the collapse period likely occurred as magma exited the crustal reservoir beneath the caldera, leading to a pressure drop and causing the roof to collapse (Gudmundsson et al., 2016). After the eruption ended, the caldera motion reverses to inflation, partly due to magma re-intruding into the crust beneath the caldera and exerting upwards pressure on the reservoir roof. Li et al. (2021) argue that viscoelastic rebound following magma withdrawal likely also contributes to the ongoing reinflation. It is believed that reversal began almost immediately post-eruption (Jónsdóttir et al., 2017; Rodríguez-Cardozo et al., 2019, Li et al., 2021), possibly as early as July 2015 (Ágústsdóttir et al., 2019). The delay until 2017 before the first teleseismically observed, large-magnitude earthquakes were detected is likely to be due to the time taken to build critical stress before rupture after the sense of deformation reversed.

During the eruption, the caldera collapse was observed to be highly asymmetrical, both in geodetic subsidence measurements and in seismic moment release (Gudmundsson et al., 2016; Ágústsdóttir et al. 2019). All events reported in the gCMT catalog during the study period are at the northern rim of the caldera, continuing this trend. Though these observations don't provide a complete picture of the ratio of seismicity and deformation, we tentatively interpret this as an indication that the asymmetric, trapdoor style mechanism continues, with the majority of fault slip occurring at the northern caldera rim.

4.2. Geometry of the Fault Plane

4.2.1. Dip

The north-south latitude-depth cross section shown in Figure 3b provides detailed insight into the geometry of the ring fault at the northern caldera rim. The relative relocations show hypocenters collapsed tightly into a band less than 2 km wide, perpendicular to the surface expression of the caldera rim, outlining a subvertical fault zone, with the best-fitting plane represented by the dashed black line. The most precise constraint on the fault planes for specific events, however, comes from the individual focal mechanisms. All well-constrained focal mechanisms in this study show a steeply dipping fault plane sub-parallel to the caldera rim. However, the rear hemisphere projection of the focal mechanisms in cross section, as seen in Figure 3b, shows that almost all of the individual fault planes dip slightly more shallowly, between 70 – 88°, southwards into the caldera. These are indicated by the half-arrows displaying slip direction. This could indicate an imbricate, block faulting style on multiple smaller fault planes, adding a piecemeal component to the trapdoor-style collapse mechanism (Acocella et al., 2007). This combination of piecemeal and trapdoor collapse has been observed in other caldera collapse events such as the recent Kilauea eruption (Anderson et al., 2019). Our results from the individual fault planes contrast with the findings of Gudmundsson et al. (2016), who report a steeply outward-dipping caldera fault on the north side of the caldera, based on a best-fit plane to hypocenters located with a sparser seismometer array. Rodríguez-Cardozo et al. (2021) find that where moment tensor solutions are close to DC (for smaller events), they indicate inward to sub-vertically dipping normal faulting on the northern caldera rim. Furthermore, when corrected for the geometry of the ring fault segment that ruptured, the CLVD moment tensor solutions for larger magnitude events also provide evidence for a sub-vertically dipping ring fault.

Hypocenter locations retrieved in this study mostly do not lie on the topographic outer caldera rim, but are located around 1 – 2 km closer to the center of the caldera. In fact, many of them align almost exactly with the trace of an inner caldera ring fault, represented by the dashed line in map view in Figure 3a and the arrow on the ice surface in Figure 3b, which was identified through InSAR imaging by Gudmundsson et al. (2016), which captured a M_W 5.3 earthquake on 2014/09/18.

4.2.2. Area of fault slip

Detailed analysis of the M_W 4.7 2017/09/07 earthquake and its aftershock sequence also provides a useful opportunity to study the area of the fault plane that slipped. The aftershock distribution will often outline the approximate area of the rupture plane for the larger magnitude “mainshock” earthquake. In Supplementary Figure S6 we outline two possible, approximate shapes of rupture plane based on the observed hypocenter distribution: one 3 x 1 km rectangle and one 3 x 3 km square. Calculations were then performed (see Supplementary Table 2) using the equation for seismic moment, given by

$$M_0 = \mu A \bar{d} \tag{1}$$

where M_0 is seismic moment, μ is the shear modulus for an elastic solid, A is fault rupture area and $\bar{d}$ is the average slip on the fault. We used a combination of possible values for each of the three variables to determine which estimates were most likely when considered in context with independent observations and additional information. Initial estimates for A come from the distribution of aftershocks from this study (Supplementary Fig. S6), varying between 3 km^2 to 9 km^2. Those for μ are from Bjarnason (2014), and references therein, who estimates a value of 10 GPa at 1.5 km depth and 32.5 GPa at 5.0 km depth; we use an intermediate value of 20 GPa as well, given that most of the hypocenters in this study lie between these two depths. Those for $\bar{d}$ are from Gudmundsson et al. (2016), varying between 1.0 – 1.5 m.

We conclude that μ likely varies between 2 – 13 GPa. It is possible that either the fault zone is weaker but with larger rupture area and/or slip, or the fault zone is stronger with rupture area and slip being at the lower end of the range of values explored.

Observations from a GPS in the center of the caldera give typically 0.3 – 0.5 m of subsidence associated with each earthquake of around M 5.2 – 5.4 that occurred during the second half of September 2014 (Fig. 3c of Gudmundsson et al., 2016). The low frequency of seismic signals from these earthquakes is also an indicator that the faults may be weaker (Bjarnason, 2014).

5. Conclusions

Motion on the caldera fault reverses; with the footwall of the caldera fault moving downwards during the eruptive period, and upwards during the post-eruptive period. This is reflected in waveforms from individual events and in the P and T axes of all events in this study. Comparison of polarity observations from co-located events during and after the eruption and precise relative relocations both indicate reversal of motion on the same ring fault structure.

Tightly constrained focal mechanisms show motion on steeply dipping faults on the northern caldera rim. Failure during individual seismic events occurs on planes dipping slightly shallower than the best fitting plane through the event hypocenters, indicating the possibility that deformation occurs in a fault zone, though this result might also be influenced by un-modelled 3D velocity structure.

Detailed analysis of the earthquake sequence surrounding a M_W 4.7 event during a period of excellent network coverage provides constraints on the size of the earthquake rupture area. This indicates that the fault likely has a relatively low shear modulus, as suggested by previous authors, and consistent with its reactivation over a short time period.

Acknowledgments

Seismometers were borrowed from the Natural Environment Research Council (NERC) SEIS-UK [loans 968 and 1022], with funding from the NERC. The Icelandic Meteorological Office (data delivery from IMO seismic database 20151001/01), Chris Bean (University College Dublin), and the British Geological Survey kindly provided additional seismic data. We thank Sveinbjörn Steinþórsson from the Institute of Earth Sciences, University of Iceland, Heidi

Soosalu and many others who assisted with fieldwork. Department of Earth Sciences, Cambridge contribution esc.nnnn.

Open Research

Seismic waveform data for all CAM stations can be downloaded from the IRIS Data Management Center. Waveform data under network codes Z7 (2010–2015, DOI: 10.7914/SN/Z7_2010) and 8K (2016–2022, DOI: 10.7914/SN/8K_2016, which is expected to become fully available by 2023) were used in this study. Waveform data from IMO stations can be accessed by request from the Icelandic Meteorological Office (https://en.vedur.is/about-imo/contact/). Additional data from the gCMT project can be found in the Global Centroid Moment Tensor database (Dziewonski et al., 1981; Ekström et al., 2012).

The catalog of events was created using QuakeMigrate (Winder et al. 2021, DOI: 10.5281/zenodo.4442749).

Data processing was completed using the following software: NonLinLoc (Lomax et al., 2000); Pyrocko and the Snuffler toolbox (Heimann et al., 2017); hypoDD (Waldhauser & Ellsworth, 2000) and MTfit (Pugh & White, 2018). Python packages and libraries ObsPy (Beyreuther et al., 2010); SciPy (Virtanen et al., 2020); NumPy (Harris et al., 2020); Pandas (Pandas development team, 2021, https://doi.org/10.5281/zenodo.3509134) and scikit-spatial (Hynes, 2019, https://github.com/ajhynes7/scikit-spatial) were also used.

Figures were produced using Matplotlib (Hunter, 2007) and Generic Mapping Tools (6.1, Wessel et al., 2019).

References

Acocella, V. (2007). Understanding caldera structure and development: An overview of analogue models compared to natural calderas. *Earth-Science Reviews, 85*(3), 125–160. https://doi.org/10.1016/j.earscirev.2007.08.004

Ágústsdóttir, T., Woods, J., Greenfield, T., Green, R. G., White, R. S., Winder, T., et al. (2016). Strike-slip faulting during the 2014 Bárðarbunga-Holuhraun dike intrusion, central Iceland. *Geophysical Research Letters*, *43,* 1495–1503. https://doi.org/10.1002/2013GL058740

Ágústsdóttir, T., Winder, T., Woods, J., White, R. S., Greenfield, T., & Brandsdóttir, B. (2019). Intense seismicity during the 2014–2015 Bárðarbunga-Holuhraun rifting event, Iceland, reveals the nature of dike-induced earthquakes and caldera collapse mechanisms. *Journal of Geophysical Research: Solid Earth*, *124*(8), 8331–8357. https://doi.org/10.1029/2018JB016010

Anderson, K. R., Johanson, I. A., Patrick, M. R., Gu, M., Segall, P., Poland, M. P., et al. (2019). Magma reservoir failure and the onset of caldera collapse at Kīlauea Volcano in 2018. *Science*, *366*(6470). https://doi.org/10.1126/science.aaz1822

Beyreuther, M., Barsch, R., Krischer, L., Megies, T., Behr, Y., & Wassermann, J. (2010). ObsPy: A Python toolbox for seismology. *Seismological Research Letters, 81*(3), 530–533. https://doi.org/10.1785/gssrl.81.3.530

Bjarnason, I. Þ. (2014). Earthquake sequence 1973–1996 in Bárðarbunga Volcano: Seismic activity leading up to eruptions in the NW-Vatnajökull area. *Jökull, 64*, 61–82.

Björnsson, H., & Einarsson, P. (1990). Volcanoes beneath Vatnajökull, Iceland: Evidence from radio echo-sounding, earthquakes and jökulhlaups. *Jökull, 40,* 147–168.

Brandsdóttir, B., & Pálsson, F. (2014). Historical accounts of 18th century eruptions possibly associated with Bárðarbunga og Grímsvötn, *Jökull*, *64,* 91–106.

Dziewonski, A. M., Chou, T.-A. &Woodhouse, J. H. (1981). Determination of earthquake source parameters from waveform data for studies of global and regional seismicity, *Journal of Geophysical Research*, *86,* 2825–2852. https://doi.org/10.1029/JB086iB04p02825

Ekström, G., Nettles, M., & Dziewoński, A. M. (2012). The global CMT project 2004–2010: Centroid-moment tensors for 13,017 earthquakes. *Physics of the Earth and Planetary Interiors, 200,* 1–9. https://doi.org/10.1016/j.pepi.2012.04.002

Grapenthin, R., Li, S., Ofeigsson, B., Sigmundsson, F., Drouin, V., Hreinsdottir, S., et al. (2018). Post-eruptive deformation after the 2014–2015 Bárðarbunga dike intrusion and rifting event, Iceland. In *EGU General Assembly Conference Abstracts 20* (pp. 15632).

Greenfield, T., White, R. S., Winder, T., & Ágústsdóttir, T. (2020). Seismicity of the Askja and Bárðarbunga volcanic systems of Iceland, 2009–2015. *Journal of Volcanology and Geothermal Research*, *391,* 106432. https://doi.org/10.1016/j.jvolgeores.2018.08.010

Gudmundsson, M. T., Jónsdóttir, K., Hooper, A., Holohan, E. P., Halldórsson, S. A., Ófeigsson, B. G., et al. (2016). Gradual caldera collapse at Bárðarbunga volcano, Iceland, regulated by lateral magma outflow. *Science*, *353*(6296), 262–271. https://doi.org/10.1126/science.aaf8988

Harris, C. R., Millman, K. J., van der Walt, S. J., Gommers, R., Virtanen, P., Cournapeau, D. et al. (2020). Array programming with NumPy. *Nature, 585*(7825), 357–362. https://doi.org/10.1038/s41586-020-2649-2

Heimann, S., Kriegerowski, M., Isken, M., Cesca, S., Daout, S., Grigoli, F. et al. (2017). Pyrocko - An open-source seismology toolbox and library. Potsdam: GFZ Data Services. https://doi.org/10.5880/GFZ.2.1.2017.001

Hunter, J. D. (2007). Matplotlib: A 2D graphics environment. *Computing in science & engineering, 9*(03), 90–95. https://doi.ieeecomputersociety.org/10.1109/MCSE.2007.55

Jóhannesson, H., & Saemundsson, K. (1998). *Jarðfræðikort af Íslandi, Höggun (Geological Map of Iceland. Tectonics)* (Scale 1:500,000). Reykjavík, Iceland: Náttúrufræðistofnun Íslands (Icelandic Institute of Natural History).

Jónasson, K., Bessason, B., Helgadóttir, Á., Einarsson, P., Gudmundsson, G. B., Brandsdóttir, B. et al. (2021). A Harmonised Instrumental Earthquake Catalogue for Iceland and the Northern Mid-Atlantic Ridge. *Natural Hazards and Earth System Sciences Discussions, 21,* 2197–2021. https://doi.org/10.5194/nhess-21-2197-2021

Jónsdóttir, K., Hooper, A., Jónasson, K., Vogfjörð, K., Gudmundsson, M. T., & Hjörleifsdóttir, V. (2017). Bárðarbunga volcano-post-eruption trends following the Holuhraun eruption in 2014–2015. In *EGU General Assembly Conference Abstracts 19* (pp. 12535).

Larsen, G., & Gudmundsson, M. T. (2015). Catalogue of Icelandic Volcanoes—Bárðarbungaa volcanic system. Available from: http:// futurevolc.vedur.is.

Li, S., Sigmundsson, F., Drouin, V., Parks, M. M., Ofeigsson, B. G., Jónsdóttir, K. et al. (2021). Ground deformation after a caldera collapse: Contributions of magma inflow and viscoelastic response to the 2015-2018 deformation field around Bárðarbunga, Iceland. *Journal of Geophysical Research: Solid Earth, 126*(3) https://doi.org/10.1029/2020jb020157

Lomax, A., Virieux, J., Volant, P., & Berge-Thierry, C. (2000). Probabilistic earthquake location in 3D and layered models. In C. Thurber and N. Rabinowitz (Eds.), *Advances in Seismic Event Location* (Vol. 18, pp.101–134). Dordrecht, Netherlands: Springer Netherlands. https://doi.org/10.1007/978-94-015-9536-0_5

Pedersen, G. B. M., Höskuldsson, A., Dürig, T., Thordarson, T., Jonsdottir, I., Riishuus, M. S. et al. (2017). Lava field evolution and emplacement dynamics of the 2014–2015 basaltic fissure eruption at Holuhraun, Iceland. *Journal of Volcanology and Geothermal Research, 340,* 155–169. https://doi.org/10.1016/j.jvolgeores.2017.02.027

Pugh, D. J., & White, R. S. (2018). MTfit: A Bayesian approach to seismic moment tensor inversion. *Seismological Research Letters, 89*(4), 1507–1513. https://doi.org/10.1785/0220170273

Rodriguez Cardozo, F. R., Hjorleifsdottir, V., Jonsdottir, K., Geirsson, H., Iglesias, A., & Franco-Sánchez, S. I. (2019). Listening to the Bárðarbunga volcano in Iceland: Studying Volcanic Earthquakes for Understanding the Past and Inferring the Future. In *AGU Fall Meeting Abstracts 2019* (pp. U13C-07).

Rodríguez-Cardozo, F., Hjörleifsdóttir, V., Jónsdóttir, K., Iglesias, A., Franco, S. I., Geirsson, H.

et al. (2021). The 2014–2015 complex collapse of the Bárðarbunga caldera, Iceland, revealed by seismic moment tensors. *Journal of Volcanology and Geothermal Research*, *416*, 107275. https://doi.org/10.1016/j.jvolgeores.2021.107275

Rögnvaldsson, S. T. and Slunga, R. (1993). Routine fault plane solutions for local networks: a test with synthetic data. *Bulletin of the Seismological Society of America*, *83*(4), 1232–1247. https://doi.org/10.1785/BSSA0830041232

Tukey, J. (1958). Bias and confidence in not quite large samples. *Annals of Mathematical Statistics*, *29*, 614.

Virtanen, P., Gommers, R., Oliphant, T. E., Haberland, M., Reddy, T., Cournapeau, D. et al. (2020). SciPy 1.0: fundamental algorithms for scientific computing in Python. *Nature methods*, *17*(3), 261–272. https://doi.org/10.1038/s41592-019-0686-2

Waldhauser, F., & Ellsworth, W. L. (2000). A double-difference earthquake location algorithm: Method and application to the northern Hayward fault, California. *Bulletin of the Seismological Society of America*, *90*(6), 1353–1368. https://doi.org/10.1785/0120000006

Wessel, P., Luis, J. F., Uieda, L., Scharroo, R., Wobbe, F., Smith, W. H. F., & Tian, D. (2019). The generic mapping tools version 6. *Geochemistry, Geophysics, Geosystems*, *20*(11), 5556–5564. https://doi.org/10.1029/2019GC008515

Winder, T., Bacon, C., Smith, J., Hudson, T., Greenfield, T., & White, R. (2020). QuakeMigrate: a modular, open-source python package for automatic earthquake detection and location. *Earth and Space Science Open Archive*. https://doi.org/10.1002/essoar.10505850.1

Winder, T., Bacon, C., Smith, J. D., Hudson, T. S., Drew, J., & White, R. S. (2021). QuakeMigrate v1. 0.0. Zenodo. DOI: 10.5281/zenodo.4442749).

Woods, J., Winder, T., White, R. S. & Brandsdóttir, B. (2019). Evolution of a lateral dike intrusion revealed by relatively relocated dike-induced earthquakes: the 2014−15 Bárðarbunga-Holuhraun rifting event, Iceland. *Earth and Planetary Science Letters*, *506*, 53–63. https://doi.org/10.1016/j.epsl.2018.10.032